ARTICLE IN PRESS

Journal of the European Ceramic Society xxx (xxxx) xxx



Contents lists available at ScienceDirect

Journal of the European Ceramic Society

journal homepage: www.elsevier.com/locate/jeurceramsoc



Integration and characterization of a ferroelectric polymer PVDF-TrFE into the grain boundary structure of ZnO via cold sintering

Javier Mena-Garcia ^{a,b}, Sinan Dursun ^b, Kosuke Tsuji ^{a,b}, Sun Hwi Bang ^{a,b}, Zhongming Fan ^b, Arnaud Ndayishimiye ^b, Clive Randall ^{a,b,*}

ARTICLE INFO

Keywords:
Cold sintering
Zinc oxide
Ferroelectric polymer
Grain boundaries

ABSTRACT

In this study, the Cold Sintering Process (CSP) is used to design ceramic-polymer composites with Polyvinylidene fluoride Trifluoroethylene (PVDF-TrFE), a ferroelectric co-polymer, as an active intergranular grain boundary phase in a semiconducting Zinc Oxide (ZnO) electroceramic matrix. The conductivity is modeled with Schottky thermionic emission and Fowler-Nordheim tunneling as a function of both temperature and voltage. In addition, through details of the dielectric characterization, the interfaces are also considered with the effective permittivity resulting with a space charge relaxation of the PVDF-TrFE. The Maxwell-Wagner-Sillars (MWS) model was used to predict ~ 3 nm as the thickness of the intergranular PVDF-TrFE phase controlling electrical properties of the composite. Transmission electron microscopy (TEM) investigation of the grain boundary phase confirms the polymer thicknesses to the dimensions predicted from the various electric measurements and subsequent modeling.

1. Introduction

Cold sintering offers unique opportunities to design composites with a wide variety of materials that are typically difficult or impossible to coprocess. Cold sintering uses a non-equilibrium thermodynamic chemomechanic process known as pressure solution creep to drive diffusion at extremely low temperatures to permit inorganic particulate materials to sinter into a dense body with over 95% theoretical densities [1]. To enable this process, a transient chemical phase along with an applied pressure and temperature is used to drive a series of consecutive mechanisms namely dissolution at the compressed contact points between particles, diffusion of solute along the grain boundaries and reprecipitation at pore surfaces, following local chemical potential gradients [2-5]. The transient phases must be carefully considered to drive the kinetics of these processes, to permit the densification at pressures from few tens of MPa, and temperatures below 400 °C [6]. Fig. 1 shows a schematic of these pressure solution creep processes enabling the low temperature sintering of the bulk materials, multilayers, or composites [7-12]. In cold sintering, various passive insulating polymers of different types have been successfully integrated at the nanometer scale into the grain boundaries. These include thermosets

such as PDMS (Polydimethylsiloxane) [13] and thermoplastics such as PTFE (Polytetrafluoroethylene) [14], PEEK (Polyether ether ketone) [15], PEI (Polyethylenimine) [16], and PPO (Poly(p-phenylene oxide) [17], among others. Here, we considered a more electrically functional co-polymer: Polyvinylidene fluoride Trifluoroethylene (PVDF-TrFE). PVDF-TrFE is a semicrystalline system with two crystalline polymorphs: a non-ferroelectric α -phase and a ferroelectric β -phase. The β -phase presents a structure that can undergo a ferroelectric to paraelectric phase transformation at $T_C \sim 124$ °C, has a relative permittivity or dielectric constant of $\epsilon_r \sim 11$ at 1 kHz, and melting point at $T_m \sim 150~^{\circ}C$ [18]. These are subject to change, depending on crystallinity and the physical confinement of PVDF-TrFE [19]. The objective of this study is to incorporate a ferroelectric polymer into the grain boundary of a densified ZnO, to form a new type of nanocomposite and investigate the associated varistor electrical properties with respect to the microstructure with physical non-linear conduction models.

https://doi.org/10.1016/j.jeurceramsoc.2022.01.064

Received 10 December 2021; Received in revised form 28 January 2022; Accepted 29 January 2022 Available online 2 February 2022

0955-2219/© 2022 Elsevier Ltd. All rights reserved.

^a Materials Science and Engineering Department, The Pennsylvania State University, University Park, PA 16802, USA

^b Materials Research Institute, Millennium Science Complex, University Park, PA 16802, USA

^{*} Corresponding author at: Materials Science and Engineering Department, The Pennsylvania State University, University Park, PA 16802, USA. *E-mail address:* car4@psu.edu (C. Randall).

2. Materials and methods

2.1. Selection of materials

2.1.1. Zinc oxide

Zinc Oxide (ZnO) is a direct wide band gap n-type semiconductor (Eg ~ 3.3 eV, Wurtzite structure, Space group P6 $_3$ mc, Point group 6 mm) which symmetry allows pyroelectric properties along < 001 >, that has attracted attention for several decades, especially because of its dielectric and semiconductor properties. The interest in ZnO for CSP investigations, lies in its recognized properties for applications in varistors, phosphors and transparent conducting films, to name a few [14,20-23].

2.1.2. PVDF-TrFE copolymer

Polyvinylidene fluoride (PVDF) and Trifluoroethylene (TrFE) are commonly used ferroelectric polymers in the electrocomponents industry [24]. The widely studied copolymer PVDF-TrFE presents a Mass average molar mass $M_W=560-880,$ Number average molar mass $M_N=190-320$ and Dispersity index $M_W/M_N=2.6-2.9$ (per 75/25 mol Arkema Piezotech FCTM 25 Data Sheet), average density $\rho=1.88$ g cm $^{-3}$ of ferroelectric to paraelectric phase transformation at $T_C\sim118$ °C, dielectric constant $\epsilon_r\sim11$ at 1 KHz for room temperature, $\epsilon_r\sim45$ at 1 MHz for T_C , and melting point at $T_m\sim150$ °C [18,25].

2.2. Experimental methods

2.2.1. Powder preparation

Zinc Oxide powder was obtained from Alfa Aesar (NanoArcTM ZN-0605) and PVDF-TrFE was obtained from PolyK Technologies (75/25 mol Arkema Piezotech FCTM 25). The PVDF-TrFE particles were cryo milled at $-196\ ^{\circ}\text{C}$ for 9 cycles of low energy (5 motions/second for 60 s) and high energy (25 motions/second for 180 s) alternating milling steps using a Retsch Cryomill. Differential Scanning Calorimetry (DSC) was conducted on the PVDF-TrFE powder as received and after the cryomilling process, using a TA Instruments Q2000 in the 40 $-170\ ^{\circ}\text{C}$ temperature range, under heating up and cooling down conditions.

2.2.2. Cold sintering process (CSP)

Dense pellets were fabricated by CSP, using 15 wt% acetic acid (2 mol/L) manually mixed with ZnO powder and 2, 6 and 10 vol% of PVDF-TrFE in an agate mortar for 10 min. The mixture was then put into a die (13 mm diameter) and uniaxially pressed at 300 MPa. The temperature of the die was increased from room temperature to 140 $^{\circ}\text{C}$ at a heating rate of 20 $^{\circ}\text{C/min}$, then maintained at 140 $^{\circ}\text{C}$ for 4 h and finally cooled down to room temperature. Representative pictures of the

powder preparation and pellet fabrication by cold sintering are shown in Fig. S1 (Supportive Information). Reported relative densities of cold sintered pellets were obtained by dividing the bulk density (determined by the geometric method) and the theoretical density of ZnO or ZnO/PVDF-TrFE composites.

2.2.3. Materials characterization

Fourier Transform Infrared (FTIR) Spectroscopy was conducted on composite cold sintered pellet with 10 vol% of PVDF-TrFE by attenuated total reflection (ATR) analysis with diamond ATR crystal. Microstructures were observed on fracture surfaces by Field Emission Scanning Electron Microscope (Thermo Fisher FESEM Verios G4) and grainboundary-grain interfaces by Transmission Electron Microscopy (TEM Talos F200X) and Energy Dispersive Spectroscopy (EDS) mapping. ZnO/ PVDF-TrFE samples were polished with a # 1200/P4000 sandpaper and ethanol. Conducting 200 nm thick Platinum electrodes were deposited using Sputter Coater (Quorum Q150R). Dielectric measurements were performed using a precision LCR meter (Keysight E4980A) at 1 MHz. The Current-Voltage (I-V) DC analysis was conducted using Hewlett-Packard 4140B pA Meter / DC Voltage source and a Trek model 10/ 10B-HS High voltage amplifier from 50 to 1000 V and temperatures in the 85-140 °C range, with incremental steps of 50 V and 5 °C, respectively.

3. Results and discussion

3.1. Fabrication of ZnO/PVDF-TrFE composite pellets by cold sintering

It is extremely important to optimize the homogeneity and control of the microstructures throughout the design of these nano-composites. So the processing steps need to be carefully considered towards this end. As an example, we considered the case of the critical processing steps for the ZnO/PVDF-TrFE composite pellets that were fabricated via CSP for volume fractions of 2, 6 and 10 vol%. For homogeneous distribution of PVDF-TrFE powder in the ZnO matrix, the PVDF-TrFE powder was cryomilled, and the average particle size decreased from 98 μm to 9 μm , as illustrated in Fig. 2. DSC was conducted on both the initial condition and the cryomilled PVDF-TrFE. Results of the DSC profiles indicated that the Curie Temperature (T_C) did not change after the particle size reduction as shown in Fig. S2. Several DSC profiles were run presenting similar results, where T_C does not change even after several heating-cooling cycles, indicating that the ferroelectric activity of the material was preserved.

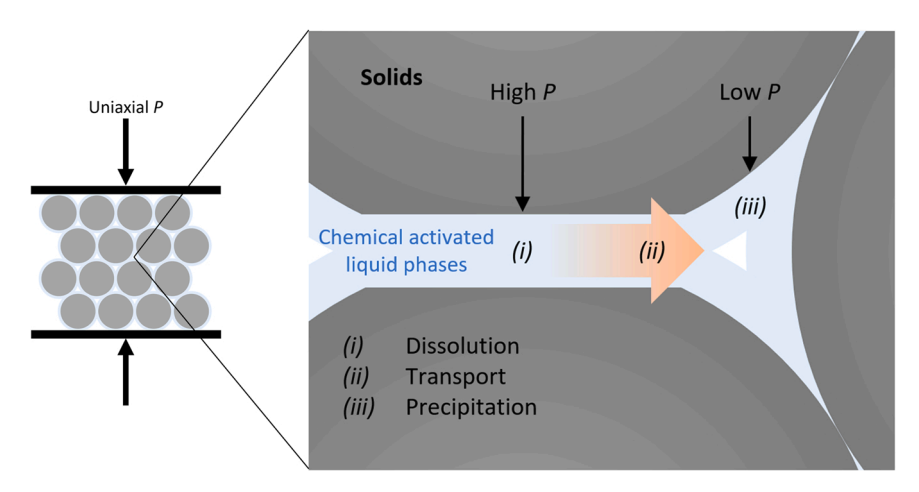


Fig. 1. Schematic illustration of the pressure solution creep mechanism that drives the sintering of bulk materials in cold sintering, adapted from Sada et al.[7] with the permission of AIP Publishing.

Fig. 2. SEM images of (a) Initial condition of ZnO powder d=142 nm, (b) initial condition of PVDF-TrFE powder d=98 μm and (c) cryomilled condition of PVDF-TrFE powder d=9 μm .

3.2. Analysis of structure-property relationships of the composites

As previously stated, a homogenous distribution of the ferroelectric polymer in the composite is primordial to accurately interpretate microstructure/properties relationship. Fig. 3 illustrates the microstructure of ZnO/PVDF-TrFE composites with different volume fractions of the polymer. Composites with a volume fraction of PVDF-TrFE of 6% and above (Fig. 3.c,d) highlight polymer segregation within the microstructure. Segregation when using high volume fraction of thermoplastic polymers was already observed in other cold sintered systems [13,14, 16]. Smaller amounts of PVDF-TrFE with good dispersion can lead to less segregation, providing an intergranular polymer barrier through the microstructure, as shown in Fig. 3b for the sample with 2 vol% PVDF-TrFE. This impacts many of the electrical properties of the composite, and these signatures of dispersed polymer can be used to aid the processing control, which can be adjusted to achieve homogeneous distribution and minimum segregation of the polymer from relative simple electrical measurements, one example being the suppression of the dielectric loss relative to the samples with no polymer, as shown in

The microstructure of the ZnO/PVDF-TrFE composite was analyzed

by Transmission Electron Microscopy (TEM) and Energy Dispersive X-Ray Spectroscopy (EDS). This analysis confirmed the integration of the polymer between the grain boundaries of ZnO grains. From the TEM image shown in Fig. 4, the grain boundary thickness can be estimated to approximatively 3 nm. However, and to be expected, segregation of polymer in pores also occurs at the larger volume fraction of 10 vol%. Such effects have been reported in earlier studies [13,14].

The cold sintered composite with 10 vol% of PVDF-TrFE was analyzed at room temperature by Fourier Transform Infrared (FTIR) spectroscopy. For the 700–1500 cm $^{-1}$ range, the peaks of the PVDF-TrFE α -phase spectrum correspond to 759, 981 and 1222 cm $^{-1}$ wavenumber values, while for the β -phase the corresponding values would be 845, 1076 and 1289 cm $^{-1}$. The corresponding vibrational assignments to these peaks are indicated in Table S1 [26,27]. The analysis in Fig. 5 indeed reveals the presence of the ferroelectric phase of the PVDF-TrFE, known as β . The presence of this β -phase is necessary for the PVDF-TrFE to be ferroelectric, however with the polymer being confined to the dimensionally constrained volumes of the grain boundary, we may expect restrained mobility of the polymer chains to this phase, leading to a shift of the Curie Temperature of phase transition [19].

Zhao et al. demonstrated that thermal activation energies for the

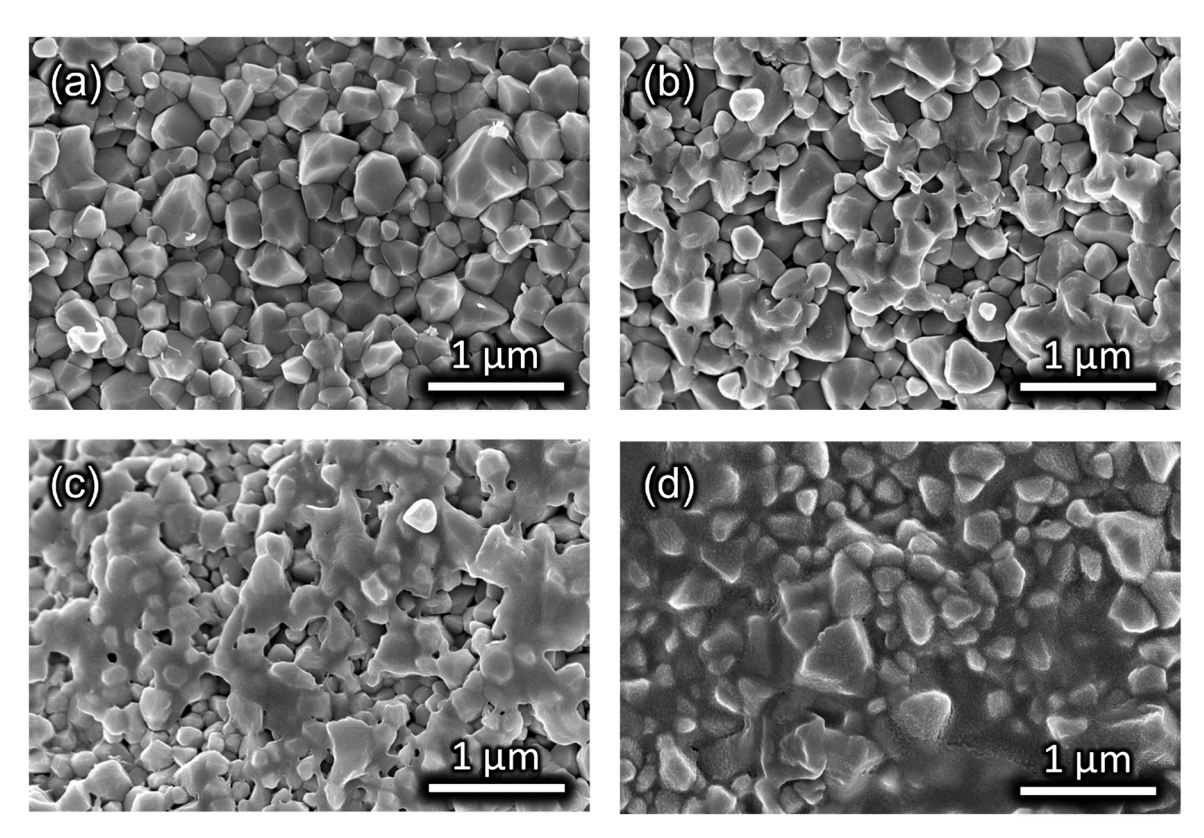


Fig. 3. Microstructure of ZnO/PVDF-TrFE composite with filler volume fractions of (a) zero vol%, (b) 2 vol%, (c) 6 vol% and (d) 10 vol%.

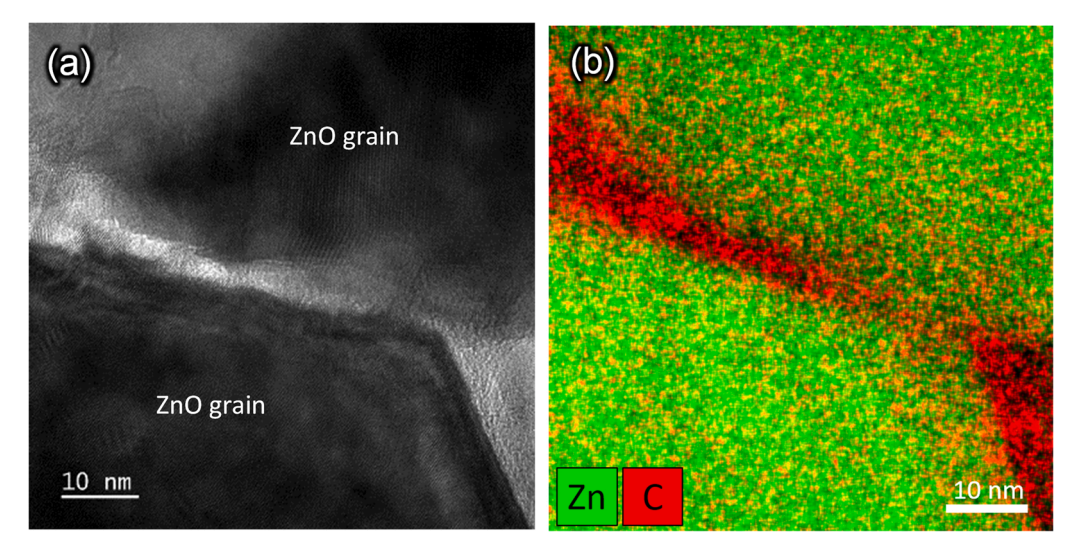


Fig. 4. (a) TEM image of PVDF-TrFE ferroelectric polymer (10 vol%) located at the interface between ZnO grains. (b) EDS mapping image showing in red the preferential presence of Carbon between the grains, confirming location of PVDF-TrFE. Note the larger segregated polymer region in the nanometric void where the grains converge toward a triple point.

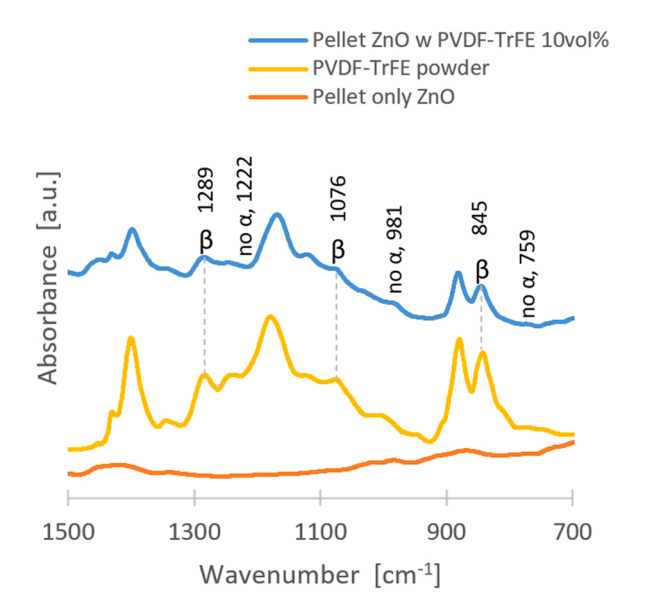


Fig. 5. FTIR spectrum of ZnO/PVDF-TrFE 10 vol% cold sintered composite, PVDF-TrFE powder and a cold sintered pellet with only ZnO.

electrical conduction at the grain boundaries of a ZnO-PTFE composite do not significantly vary for polymer content above 0.5 vol%. This phenomenon is attributed to the fact that the matrix ZnO has to densify and there can only be a limited amount of polymer confinement otherwise this would limit the cold sintering densification. In addition, these polymers confined at nanometric dimensions between the adjacent grains will possibly experience restrain to the mobility of polymer chains in the β -phase to reorient in the presence of an applied electric field, and to switch their structure during phase transformation from β to α phase, for this PVDF-TrFE material [14]. Earlier, Tsutsumi et al. reported the depression of crystallinity and repression of molecular mobility of confined PVDF-TrFE thin films for thickness under 100 nm [19]. However with thermal annealing at 150 °C the crystallinity and the ferroelectric properties improved at least at 20 nm thicknesses. Despite the nanometer scales observed here, it appears that with the cold sintering temperatures the ferroelectric properties are stable. In the following section, the dielectric measurements of the cold sintered composites support that there were no limitations to the formation of the β -phase, as

no shift of the Curie point was observed.

3.2.1. Dielectric characterization

Characterization of electrical properties was conducted on ZnO samples with zero, 2, 6 and 10 vol% of PVDF-TrFE. All samples containing the mentioned volume fractions of PVDF-TrFE exhibited a peak of relative permittivity values at the ferroelectric-paraelectric $T_{C}\sim124\,^{\circ}\text{C}$, consistent with the ferroelectric properties of the polymer after CSP. This characteristic peak of the relative permittivity, along with suppression of dielectric loss are shown in Fig. 6 for measurements at 1 MHz of sample containing 10 vol% of PVDF-TrFE.

Considering the dielectric data as a function of frequency and temperature the dielectric response has a strong relaxation behavior that is consistent with space charge polarization. The space charge being the result of the semiconducting ZnO grains and the insulating polymer acting as barriers at each grain boundary. Thermal Activation Energies (E_A) were determined from dielectric relaxations (ε_r '') measured as a function of frequencies (from 1 kHz to 1 MHz), from the Arrhenius Eq. 2.1.

$$\omega_r = \omega_0 \quad exp\left(\frac{-E_A}{k_B T}\right)$$
 (Eq. 3.1)

Fig. 7 shows that the calculated Activation Energies did not vary significantly ($E_A \sim 0.4$ eV) among the samples with 2 vol%, 6 vol% and 10 vol% of filler (standard least squares error of the estimates = 0.23, 0.20 and 0.34 rad/s, respectively).

The Maxwell-Wagner-Sillars (MWS) effect is a mechanism that describes interfacial space charge contributions to dielectric loss as a function of frequency, due to the charge buildup at the electrode/sample interface. Thereby the segregated polymer in pores has less impact on the overall dielectric properties than the serial distribution of the intergranular PVDF-TrFE. Therefore, we can approximate the relaxation frequency with the MWS model. The peak frequency f_{MWS} describes the polarization present at internal boundary layers within an inhomogeneous sample [28,29] and is given by Eq. 3.2:

$$f_{MWS} = \frac{\sigma_{sam}}{2\pi\varepsilon_0(\varepsilon'_{sam} + (l_{sam}/l_{ins})\varepsilon'_{ins})}$$
(Eq. 3.2)

where ε'_{sam} , ε'_{ins} , l_{sam} and l_{ins} correspond to the real permittivities, grain size and insulating intergranular polymer grain boundary layers, respectively.

Taking for example the case of the ZnO/PVDF-TrFE (10 vol%)

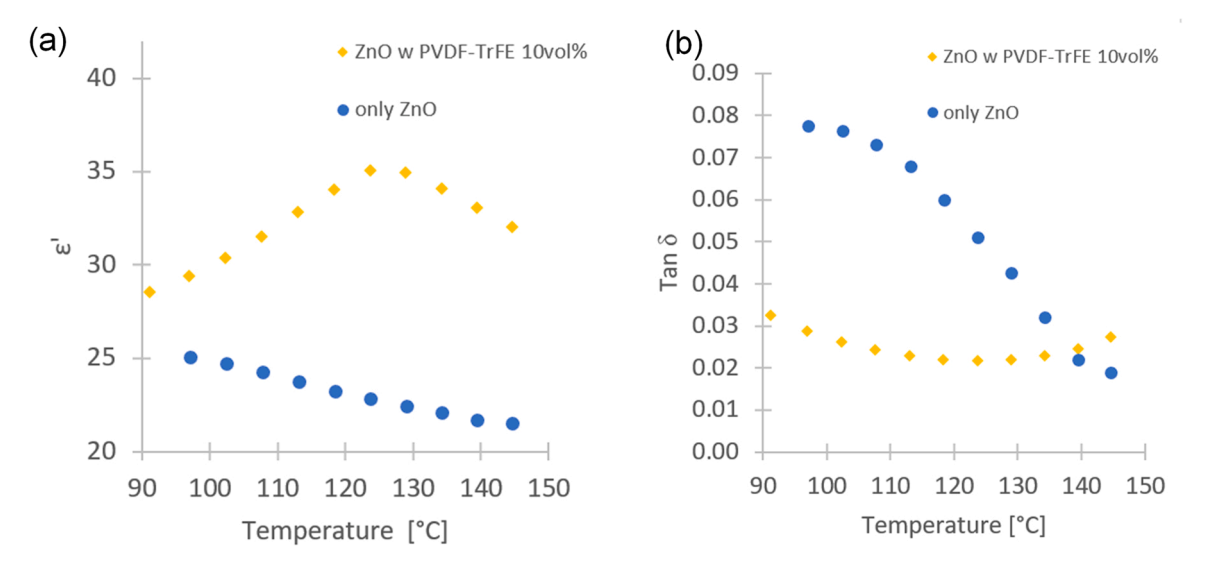


Fig. 6. (a) Relative permittivity and (b) Tan δ values for ZnO/PVDF-TrFE composites as a function of temperature and under heating at 1 MHz.

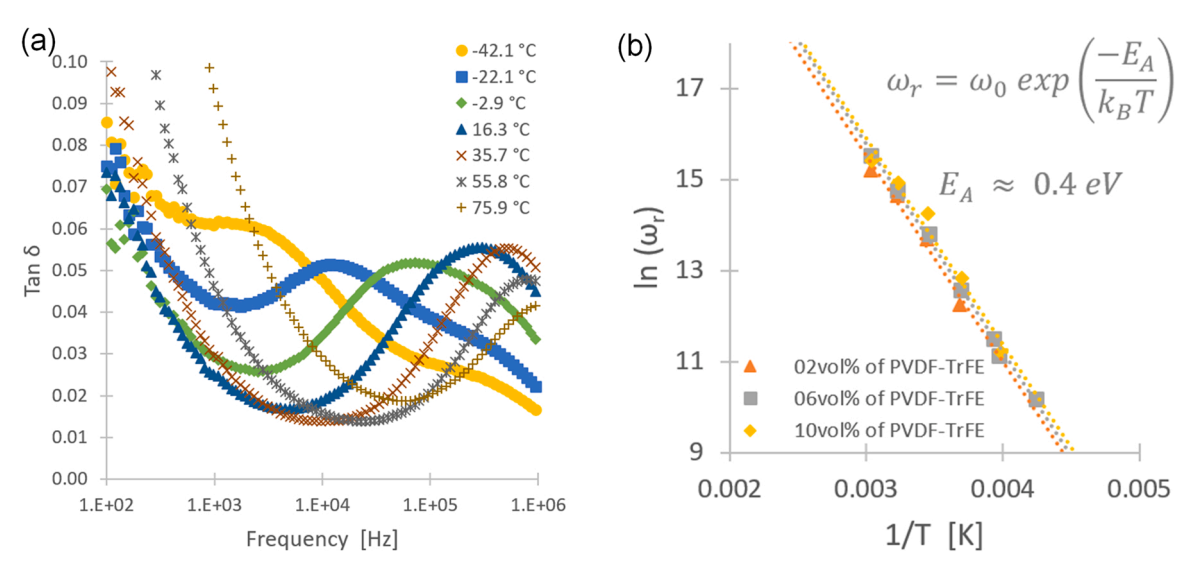


Fig. 7. (a) Dielectric relaxations (ϵ_r '') of ZnO/PVDF-TrFE 10 vol% composite, and (b) corresponding Arrhenius plot illustrating determination of thermal activation energies for 2, 6 and 10 vol%.

composite, the relaxation frequency $f_{MWS} \sim 4.83 \times 10^5 Hz$ (illustrated in Fig. 7.a), is used as verification method for the average grain boundary layer thickness throughout the bulk sample. When the values $\varepsilon'_{sam} = \varepsilon'_{ZnO} = 10$, $\varepsilon'_{ins} = \varepsilon'_{PVDF-TrFE} = 11$, $\sigma_{sam} = \sigma_{ZnO} = 3 \times 10^{-2} \ \Omega^{-1} m^{-1}$, $\varepsilon_0 = 8.854 \times 10^{-12} s \Omega^{-1} m^{-1}$ and $l_{sam} \sim 300 nm$ (grain size) are introduced in Eq. 3.2, a computed value of the average grain boundary thickness $l_{ins} \sim 2.9 nm$ is obtained, and this is consistent with the TEM observation, as grain boundary thicknesses of $\delta_{PVDF-TrFE}$ is approximatively 3 nm as illustrated in Fig. 4a.

3.2.2. Current-Voltage (I-V) analysis

Zinc Oxide is one of the most frequently used materials for the fabrication of Voltage-Dependent Resistors (VDR), also commonly known as Varistors. This type of electronic component is used to protect a circuit connected in parallel from high voltage discharges, and it does so by varying its resistance value in response to the magnitude of the applied voltage. Miller, Moulson and Herbert, Mahan, Levinson and Philipp, have extensively studied and reported the relation between the structure and properties, including the conduction mechanisms of ZnO VDRs.[14,30–33] Collectively, they have defined the Current-Voltage

(I-V) non-ohmic response of VDRs by Eq. 3.3:

$$I = KV^{\alpha} \tag{Eq. 3.3}$$

where I is the current, V is the applied voltage, K is a proportional constant and α is the exponential term corresponding to the non-linear response.

The VDR behavior of ZnO arises from the grain boundaries acting as acceptors for the electrons from n-type donors in the semiconductor grains. This can be interpreted as two Schottky barriers oppositely oriented on each side of the intergranular layer (IGL), to prevent the flow of electrons from one grain to its neighboring one. Therefore, when a voltage is applied to the varistor element, electrons flow from the grain to the IGL at the forward biased junction, while at the reversed biased junction thermally activated electrons will flow from IGL into the grain at low voltages, and electrons will tunnel in the same direction at high voltages [21,29,34,35].

The flow of thermally activated electrons that occurs in the reverse biased junction at low voltages can be described by the Schottky Thermionic Emission phenomenon by Eq. 3.4:

$$J = AT^{2} \exp[\overline{f_{0}}] \frac{(\beta E_{GB}^{1/2} - q\Phi_{B})}{k_{B}T}$$
 (Eq. 3.4)

where J is the current density, A is a proportionality constant, T is the temperature, β is determined by the slope (= β/k_BT) in the Schottky Emission plot (ln(J/T²) vs $E_{GB}^{1/2}$), E_{GB} is the applied Electric field and $q\phi_B$ is the Schottky barrier height. The $q\phi_B$ can be calculated from Eq. 3.4 at $E_{GB}\!=\!0$.

For high voltages, the quantum mechanism known as Fowler-Nordheim tunneling takes place allowing the flow of electrons from the IGL into the ZnO grain at the reverse biased junction. This quantum conduction mechanism is described by Eqs. 3.5 and 3.6:

$$J = AE_{GB}^2 \exp[f_0](-\gamma/E_{GB})$$
 (Eq. 3.5)

$$\gamma = \frac{8\pi\sqrt{2m^*}}{3ah}(q\varphi_B)^{3/2}$$
 (Eq. 3.6)

The PVDF based barriers are expected to give non-linear conduction processes across the composite. Electrical characterization revealed an enhancement on the non-ohmic response with the addition of the ferroelectric polymer (Fig. S4). The α values from the I-V analysis in Fig. 8 were 1.3 and 3.5 at 120 °C for the pellets containing zero and 2 vol % of PVDF-TrFE, only increasing marginally to $\sim\!4.0$ with 10 vol% of the polymer. Therefore, we provide a more detailed analysis of the composite with 2 vol% PVDF-TrFE.

Considering the calculated activation energies for the dielectric relaxation of the ZnO/PVDF-TrFE reported in Fig. 7.b of this work and noting these did not significantly vary for the different amounts of polymer amount in the composite, to a first order approximation we can use bulk PVDF-TrFE properties to consider more details of the composite, as applied below, into the parameterization of the dielectric media at the interfaces.

To determine the electronic conduction mechanism across the grain boundaries of the composite material, the applied electric field should be calculated per grain boundary length E_{GB} according to Eq. 3.7:

$$E_{GB} = E \frac{d}{\tilde{s}}$$
 (Eq. 3.7)

where E is the applied electric field, d is the average grain size and δ is the depletion layer or grain boundary thickness. For this analyzed system, d \sim 293 nm and $\delta\sim$ 3 nm.

3.2.2.1. Low voltage analysis. At low applied voltage, the electronic conduction mechanism could be Schottky thermionic emission, Poole-Frenkel emission or a combination of both mechanisms. To determine which mechanism is dominating the electronic conduction in the

system, the natural logarithm of current density (J) over temperature squared (T^2), and the natural logarithm of current density (J) over applied electric field (E_{GB}), must be plotted as function of square root of the applied electric field ($E_{GB}^{0.5}$). The calculated slope values, corresponding to the data points trending linearly in the ln (J/ T^2) as function of $E_{GB}^{0.5}$ for Schottky Emission, and in the n (J/ E_{GB}) as function of $E_{GB}^{0.5}$ for Poole-Frenkel, are then used to determine each β value by $E_{QB}^{0.5}$.

$$slope = \frac{\beta}{k_B T}$$
 (Eq. 3.8)

where k_B is Boltzmann's constant. The η value is 4 for a Schottky thermionic emission ($\eta_{\text{P-F}} = 4$) and 1 for Poole-Frenkel emission ($\eta_{\text{P-F}} = 1$) [35,38,39], and it is calculated by Eq. 3.9:

$$\eta = \frac{q^3}{\beta^2 \pi \varepsilon_0 \varepsilon_\infty} \tag{Eq. 3.9}$$

where q is the fundamental electric charge and ε_{∞} is the dynamic permittivit ($\equiv n^2$).

The plots illustrated in Fig. 9 show the slope of linear response at low voltages used to determine $\eta_{S\text{-E}}$ and $\eta_{P\text{-F}}$. To calculate η using Eq. 3.9, the considered value of the dynamic permittivity was the refractive index squared of the ferroelectric polymer in the 0.5 – 2.5 THz frequency range, $\epsilon_{\infty} \rightarrow \epsilon_{r}$ PVDF-TrFE(0.5–2.5 THz) = 3. The electron transport across an insulating polymer media would be expected to have a slower mobility, and therefore the refractive index would be more appropriately taken from the THz frequency range than the optical [40].

The computed η_{S-E} values were between 4.9 and 10.2 for a temperature range from 120 °C to 85 °C; and between 36.9 and 504.5 for η_{P-F} within the same temperature range. Both S-E and P-F conduction mechanisms are well known field-assisted thermally stimulated processes. With temperature rise, the electron's energy increases to cross the insulating grain boundary by Schottky thermionic emission due to the applied field and image force; similarly, in the Poole-Frenkel mechanism the temperature rise facilitates the thermal detrapping of an electron from the bulk material into the conduction band [38]. Consequently, as the temperature increases, the η_{S-E} and η_{P-F} values approach to 4 and 1 respectively. Therefore, these results indicate the Schottky thermionic emission to be the dominating conduction mechanism over Poole-Frenkel, between grain boundaries at low voltages. From Eq. 3.4 at E_{GB} = 0, the Schottky barrier height was calculated to be $q\phi_B = 1.1$ eV for the ZnO with 2 vol% of PVDF-TrFE composite.

(see Table 1).

The Current-Voltage-Temperature data in Fig. 9 allow to describe the low field behavior with the Schottky-Emission conduction across the grain boundaries as η clearly matches the expected values of 4, relative to the values of Poole-Frenkel where $\eta=1$, and our experimental data

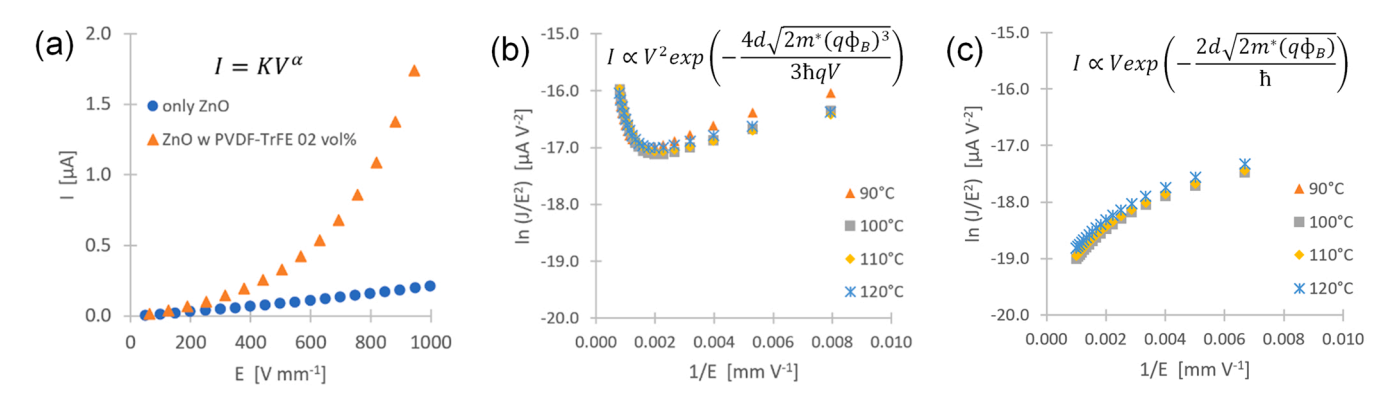
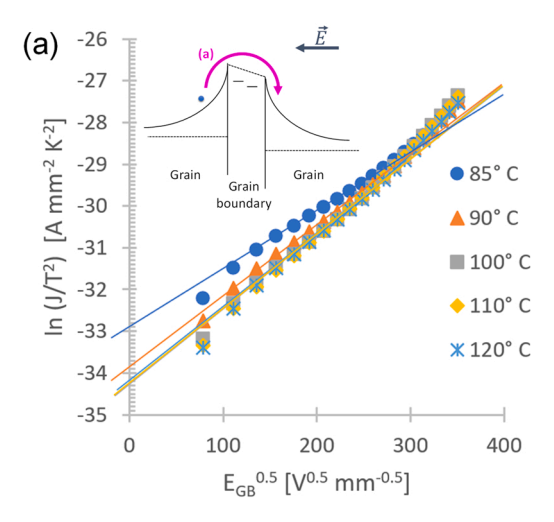


Fig. 8. (a) Current as a function of applied Electric field shows an enhance in the non-ohmic response of composite sample, contrasting with the near to linear α coefficient value for the pure ZnO polycrystalline pellet. (b) Current density as a function of reciprocal applied Electric field shows an increase at higher voltage values presenting a Fowler-Nordheim characteristic, here shown for the ZnO/PVDF-TrFE composite with 2 vol% filler. (c) Response to I-V measurements from pure ZnO polycrystalline sample, presenting a direct tunneling behavior characteristic of a trapezoidal tunneling barrier [36,37].



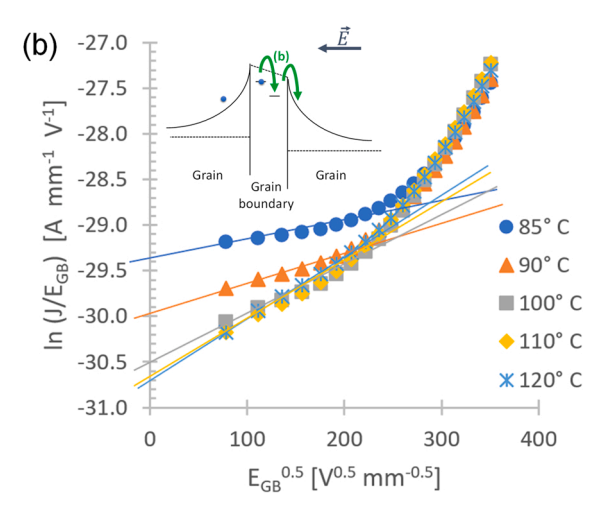


Fig. 9. (a) Schottky Emission plot and (b) Poole-Frenkel plot, from ZnO/PVDF-TrFE (2 vol% filler) composite (diagrams of Schottky Emission and Poole-Frenkel mechanisms based on model of Mahan et al. [33,35]).

Table 1 Calculated η values in the 85 – 120 $^{\circ}\text{C}$ temperature range.

Temperature	$\eta_{S\text{-}E}$	Standard least squares error of the estimate $[A mm^{-2} K^{-2}]$	$\eta_{P\text{-}F}$	Standard least squares error of the estimate $[A mm^{-1} V^{-1}]$
85 °C	10.2	±0.016	504.5	±0.026
90 °C	7.3	± 0.025	157.8	± 0.036
100 °C	5.3	± 0.034	69.7	± 0.043
110 °C	4.7	± 0.023	43.5	± 0.038
120 °C	4.9	± 0.015	36.9	± 0.016

under this analysis was far off those values, thereby leading to the conclusion that the non-linear conduction is best described by the Schottky-Emission mechanism.

3.2.2.2. High voltage analysis. The nature of the conduction changes at higher fields, and the cross over can be readily seen in the form of a Fowler-Nordheim plot for these composites. The Fowler-Nordheim plot in Fig. 10 shows the fitting linear response at high applied voltages, which correlates values of $\gamma=0.166~V/nm=0.166~\times~10^9~J~C^{-1}~m^{-1}$ (standard error of the estimate $=0.081~A~V^{-2}$), with $A=4\times10^{-17}~from$ Eq. 3.5. Using Eq. 3.6, considering an effective mass of $m^*_{ZnO}=0.23~m_0$, [41] and being $m_0=8.187\times10^{-14}~J~c^{-2}~due$ to the interatomic

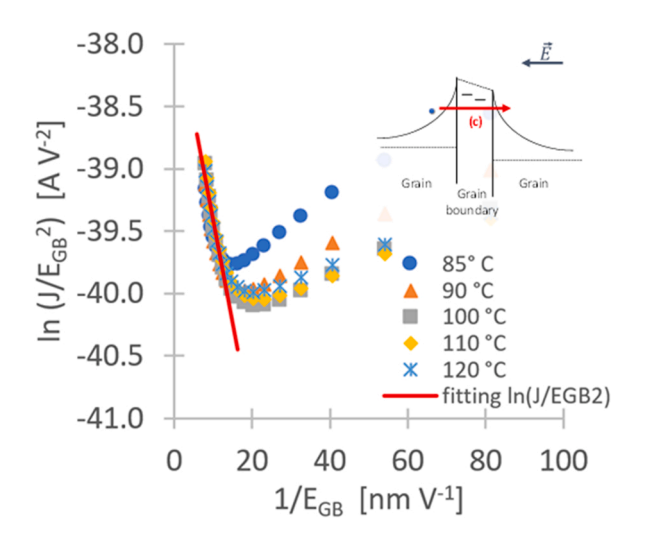


Fig. 10. Fowler-Nordheim plot from ZnO/PVDF-TrFE (2 vol% filler) composite (diagram of tunneling mechanism based on model of Mahan et al.[33,35]).

potentials that influence the electron momentum under conduction, the calculated barrier height of the Fowler-Nordheim tunneling is $q\phi_B=0.1\ eV$ at high fields.

3.2.3. Barrier height field dependence

Jinliang He [42] established that, in a general form, the field dependence of the barrier height at the grain boundaries for ZnO varistors can be expressed by Eq. 3.10:

$$q\varphi_B = \frac{E_c}{4} \left(1 - \frac{E_{GB}}{E_c} \right)^2, \quad E_{GB} \le E_c$$
 (Eq. 3.10)

where E_{GB} is the applied electric field at the grain boundary and E_c is a critical voltage at which the barrier height vanishes as illustrated in Fig. 11. Here we consider this dependence under the Fowler-Nordheim tunneling conduction described by Eq. 3.11 and also the Schottky Emission conduction described by Eq. 3.12:

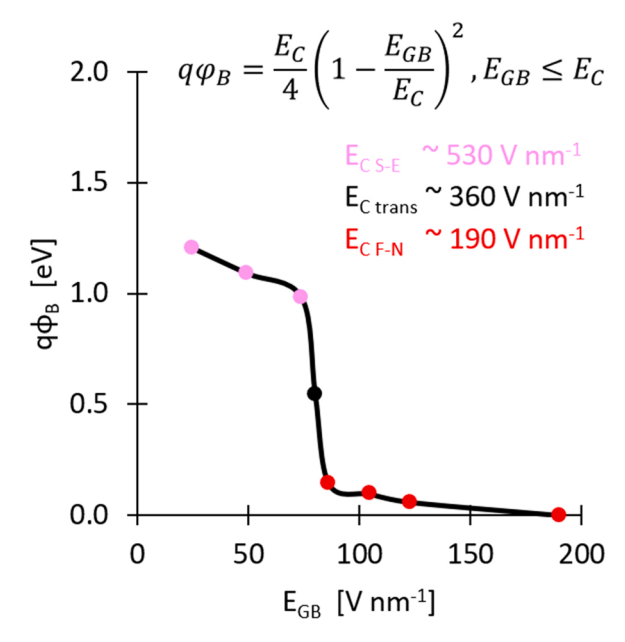


Fig. 11. Barrier height as a function of applied Electric field at the grain boundaries, shows a decreasing behavior in correlation with Eq. 3.10 and its corresponding schematic from Blatter and Greuter[43].

$$q\varphi_{B}^{F-N} = \frac{E_{c}^{F-N}}{4} \left(1 - \frac{E_{GB}}{E_{c}^{F-N}}\right)^{2}, \quad E_{GB} \leq E_{c}^{F-N} \tag{Eq. 3.11}$$

$$q\varphi_B^{S-E} = \frac{E_c^{S-E}}{4} \left(1 - \frac{E_{GB}}{E_c^{S-E}}\right)^2, \quad E_{GB} \le E_c^{S-E}$$
 (Eq. 3.12)

where $E_c^{F-N} \sim 190$ V/nm and $E_c^{S-E} \sim 530$ V/nm. This coincides with the smaller barrier height obtained at high applied voltages (0.1 eV for Fowler-Nordheim conduction), compared to the larger barrier height at low applied voltages (1.1 eV for Schottky emission). The transition regime was also considered, averaging $E_c^{trans} \sim 360$ V/nm and a with a barrier height corresponding calculated value $q\varphi_R^{trans} \sim 0.5$ eV.

By considering the results obtained in these analyses of the electrical characterization of ZnO/PVDF-TrFE composite, it is noticeable that the preservation of the ferroelectric properties of the polymer integrated at the grain boundaries enables the Fowler-Nordheim tunneling conduction mechanism in contrast with the direct tunneling characteristic of the only ZnO sample, as shown in Fig. 8.b,c. Additionally, it was observed that the barrier height at the grain boundaries decreases at higher applied Electric fields as described by He[42] and Blatter and Greuter[43], as illustrated in Fig. 11. These features are valuable to asses for new application opportunities of electroceramics in varistors, energy harvesting and actuators on flexible substrates.

4. Conclusions

The cold sintering process enabled the fabrication of ZnO/PVDF-TrFE ceramic-polymer composite samples to relative densities > 95% for volume fractions of 2, 6 and 10 vol% at temperatures as low as 140 °C. Through a TEM analysis the thickness of the PVDF-TrFE to be \sim 3 nm at grain boundaries. The ferroelectric properties of PVDF-TrFE were preserved after the cold sintering process within these confined regimes, this being demonstrated by the presence of the polymer's β phase peaks in FTIR spectroscopy and by the anomaly of the composite dielectric permittivity maxima at $T_C \sim 124\,^{\circ}C$. From the frequency dependence at different temperatures the relaxation could be correlated via the Maxwell-Wagner-Sillars (MWS) effect using the f_{MWS} relaxation frequency identified in dielectric measurements of imaginary permittivity. This provides a calculated barrier thickness with all the expected physical properties of the ZnO and the PVDF-TrFE in good agreement with TEM observations. To better understand the nature of the conduction across these grain boundaries, a more comprehensive currentvoltage (I-V) analysis performed on ZnO-PVDF-TrFE composites revealed a non-ohmic behavior, indicating at low voltages applied, a conduction mechanism across grain boundaries of Schottky thermionic emission with a barrier height of 1.1 eV. At higher voltages the conduction transitions to a Fowler-Nordheim tunneling with effectively reducing of the barrier to 0.1 eV. The field dependence of the barrier height is also tested with a phenomenological model. This study points to the ability to introduce functional polymers into the grain boundaries of ceramics, and correlate physical trends in the properties.

Declaration of Competing Interest

The authors declare that they have no known competing financial interests or personal relationships that could have appeared to influence the work reported in this paper.

Acknowledgments

This material is based upon work supported by the National Science Foundation, as part of the Center for Dielectrics and Piezoelectrics under Grant Nos. IIP-1841453 and IIP-1841466. We would like to acknowledge the staff of the Materials Characterization Laboratory at The Pennsylvania State University, for aiding in the work described here and

for the use of their equipment. We thank Joanne Aller for her help to prepare the manuscript. The author (J.M.) also thanks Mr. Zane Grady for helpful discussions. We also thank the members of the many companies that continue to offer support and ideas to drive this work.

Appendix A. Supporting information

Supplementary data associated with this article can be found in the online version at doi:10.1016/j.jeurceramsoc.2022.01.064.

References

- [1] J. Guo, H. Guo, A.L. Baker, M.T. Lanagan, E.R. Kupp, G.L. Messing, C.A. Randall, Cold sintering: a paradigm shift for processing and integration of ceramics, Angew. Chem. Int. Ed. 55 (2016) 11457–11461, https://doi.org/10.1002/anie.201605443.
- [2] F. Bouville, A.R. Studart, Geologically-inspired strong bulk ceramics made with water at room temperature, Nat. Commun. 8 (2017), https://doi.org/10.1038/ ncomms14655.
- [3] J.P. Gratier, D.K. Dysthe, F. Renard, The Role of Pressure Solution Creep in the Ductility of the Earth's Upper Crust, Elsevier Inc, 2013, https://doi.org/10.1016/ B978-0-12-380940-7.00002-0.
- [4] X. Zhang, C.J. Spiers, C.J. Peach, Compaction creep of wet granular calcite by pressure solution at 28°C to 150°C, J. Geophys. Res. Solid Earth 115 (2010) 1–18, https://doi.org/10.1029/2008JB005853.
- [5] A. Ndayishimiye, M.Y. Sengul, T. Sada, S. Dursun, S.H. Bang, Z.A. Grady, K. Tsuji, S. Funahashi, A.C.T. van Duin, C.A. Randall, Roadmap for densification in cold sintering: chemical pathways, Open Ceram. 2 (2020), 100019, https://doi.org/ 10.1016/j.oceram.2020.100019.
- [6] S.H. Bang, A. Ndayishimiye, C.A. Randall, Anisothermal densification kinetics of the cold sintering process below 150 °C, J. Mater. Chem. C 8 (2020) 5668–5672, https://doi.org/10.1039/d0tc00395f.
- [7] T. Sada, A. Ndayishimiye, Z. Fan, Y. Fujioka, C.A. Randall, Surface modification of BaTiO₃ with catechol surfactant and effects on cold sintering, J. Appl. Phys. 129 (2021), https://doi.org/10.1063/5.0049905.
- [8] S. Grasso, M. Biesuz, L. Zoli, G. Taveri, A.I. Duff, D. Ke, A. Jiang, M.J. Reece, A review of cold sintering processes, Adv. Appl. Ceram. 119 (2020) 115–143, https://doi.org/10.1080/17436753.2019.1706825.
- [9] J.A. Liu, C.H. Li, J.J. Shan, J.M. Wu, R.F. Gui, Y.S. Shi, Preparation of high-density InGaZnO₄ target by the assistance of cold sintering, Mater. Sci. Semicond. Process. 84 (2018) 17–23, https://doi.org/10.1016/j.mssp.2018.04.030.
- [10] X. Kang, R. Floyd, S. Lowum, M. Cabral, E. Dickey, J.P. Maria, Mechanism studies of hydrothermal cold sintering of zinc oxide at near room temperature, J. Am. Ceram. Soc. 102 (2019) 4459-4469, https://doi.org/10.1111/jace.16340.
- [11] I.J. Induja, M.T. Sebastian, Microwave dielectric properties of mineral sillimanite obtained by conventional and cold sintering process, J. Eur. Ceram. Soc. 37 (2017) 2143–2147, https://doi.org/10.1016/j.jeurceramsoc.2017.01.007.
- [12] Y. Liu, Q. Sun, D. Wang, K. Adair, J. Liang, X. Sun, Development of the cold sintering process and its application in solid-state lithium batteries, J. Power Sources 393 (2018) 193–203, https://doi.org/10.1016/j.jpowsour.2018.05.015.
- [13] A. Ndayishimiye, Z.A. Grady, K. Tsuji, K. Wang, S.H. Bang, C.A. Randall, Thermosetting polymers in cold sintering: the fabrication of ZnOpolydimethylsiloxane composites, J. Am. Ceram. Soc. 103 (2020) 3039–3050, https://doi.org/10.1111/jace.17009.
- [14] X. Zhao, J. Guo, K. Wang, T. Herisson De Beauvoir, B. Li, C.A. Randall, Introducing a ZnO–PTFE (Polymer) nanocomposite varistor via the cold sintering process, Adv. Eng. Mater. 20 (2018) 1–8, https://doi.org/10.1002/adem.201700902.
- [15] M. Si, J. Hao, E. Zhao, X. Zhao, J. Guo, H. Wang, C.A. Randall, Preparation of zinc oxide/poly-ether-ether-ketone (PEEK) composites via the cold sintering process, Acta Mater. 215 (2021), 117036, https://doi.org/10.1016/j. actamat.2021.117036.
- [16] J. Guo, N. Pfeiffenberger, A. Beese, A. Rhoades, L. Gao, A. Baker, K. Wang, A. Bolvari, C.A. Randall, Cold sintering Na₂Mo₂O₇ ceramic with poly(ether imide) (PEI) polymer to realize high-performance composites and integrated multilayer circuits, ACS Appl. Nano Mater. 1 (2018) 3837–3844, https://doi.org/10.1021/ acsanm.8b00609.
- [17] T. Sada, K. Tsuji, A. Ndayishimiye, Z. Fan, Y. Fujioka, C.A. Randall, Highly reliable BaTiO₃ –polyphenylene oxide nanocomposite dielectrics via cold sintering, Adv. Mater. Interfaces 8 (18) (2021) 1–11. https://doi.org/10.1002/admi.202100963.
- [18] Q.M. Zhang, V. Bharti, X. Zhao, Giant electrostriction and relaxor ferroelectric behavior in electron- irradiated poly(vinylidene fluoride-trifluoroethylene) copolymer, Science 280 (1998) 2101–2104, https://doi.org/10.1126/ science 280 5372 2101
- [19] N. Tsutsumi, A. Ueyasu, W. Sakai, C.K. Chiang, Crystalline structures and ferroelectric properties of ultrathin films of vinylidene fluoride and trifluoroethylene copolymer, Thin Solid Films 483 (2005) 340–345, https://doi. org/10.1016/j.tsf.2004.12.033.
- [20] Ü. Özgür, Y.I. Alivov, C. Liu, A. Teke, M.A. Reshchikov, S. Doğan, V. Avrutin, S. J. Cho, H. Morko, A comprehensive review of ZnO materials and devices, in: J. Appl. Phys., 98, 2005, pp. 1–103, https://doi.org/10.1063/1.1992666.
- [21] J. Guo, B. Legum, B. Anasori, K. Wang, P. Lelyukh, Y. Gogotsi, C.A. Randall, Cold sintered ceramic nanocomposites of 2D MXene and zinc oxide, Adv. Mater. 30 (2018) 1–6, https://doi.org/10.1002/adma.201801846.

- [22] J.P. Maria, X. Kang, R.D. Floyd, E.C. Dickey, H. Guo, J. Guo, A. Baker, S. Funihashi, C.A. Randall, Cold sintering: current status and prospects, J. Mater. Res. 32 (2017) 3205–3218, https://doi.org/10.1557/jmr.2017.262.
- [23] H. Moriwake, A. Konishi, T. Ogawa, K. Fujimura, C.A.J. Fisher, A. Kuwabara, T. Shimizu, S. Yasui, M. Itoh, Ferroelectricity in wurtzite structure simple chalcogenide, Appl. Phys. Lett. 104 (2014) 1–4, https://doi.org/10.1063/ 1.4884596.
- [24] L.S. Miller, J.B. Mullin, Electronic Materials from Silicon to Organics, Springer Science Business Media, New York, 1991. https://doi.org/10.1007/ 978-1-4615-3818-9.
- [25] N.A. Nazir, N. Kim, W.G. Iglesias, A. Jakli, T. Kyu, Conductive behavior in relation to domain morphology and phase diagram of Nafion/poly(vinylidene-cotrifluoroethylene) blends, Polymers 53 (2012) 196–204, https://doi.org/10.1016/ i.polymer.2011.11.019.
- [26] A. Árrigoni, L. Brambilla, C. Bertarelli, G. Serra, M. Tommasini, C. Castiglioni, P (VDF-TrFE) nanofibers: Structure of the ferroelectric and paraelectric phases through IR and Raman spectroscopies, RSC Adv. 10 (2020) 37779–37796, https://doi.org/10.1039/d0ra05478i.
- [27] A. Milani, C. Castiglioni, S. Radice, Joint experimental and computational investigation of the structural and spectroscopic properties of poly(vinylidene fluoride) polymorphs, J. Phys. Chem. B 119 (2015) 4888–4897, https://doi.org/ 10.1021/acs.jpcb.5b00161.
- [28] A.K. Jonscher, Dielectric relaxation in solids, Chelsea, Dielectr. Pub., London. (1983)
- [29] J.R. Macdonald, E. Barsoukov, Impedance Spectroscopy: Theory, Experiment and Applications, second ed., Wiley-Interscience, Hoboken, New Jersey, 2005.
- [30] J.M. Moulson, A.J. Herbert, Electroceramics, second ed., John Wiley & Sons Ltd, West Sussex, England, 2003.
- [31] P.H. Miller, The electrical conductivity of zinc oxide, Phys. Rev. 60 (1941) 890–895, https://doi.org/10.1103/PhysRev.60.890.
- [32] L.M. Levinson, H.R. Philipp, Zinc oxide varistors a review, Am. Ceram. Soc. Bull. 65 (1986) 639–646.
- [33] G.D. Mahan, L.M. Levinson, H.R. Philipp, Theory of conduction in ZnO varistors, J. Appl. Phys. 50 (1979) 2799–2812, https://doi.org/10.1063/1.326191.

- [34] F.C. Chiu, A review on conduction mechanisms in dielectric films, Adv. Mater. Sci. Eng. 2014 (2014) 1–18, https://doi.org/10.1155/2014/578168.
- [35] K. Tsuji, W. Chen, H. Guo, W. Lee, C.A. Randall, S. Guillemet, Contrasting conduction mechanisms of two internal barrier layer capacitors: (Mn, Nb) -doped SrTiO₃ and CaCu₃Ti₄O₁₂, J. Appl. Phys. 121 (2017), https://doi.org/10.1063/ 1.4976011 hal-02403341.
- [36] J.M. Beebe, B. Kim, J.W. Gadzuk, C.D. Frisbie, J.G. Kushmerick, Transition from direct tunneling to field emission in metal-molecule-metal junctions, Phys. Rev. Lett. 97 (2006), 026801, https://doi.org/10.1103/PhysRevLett.97.026801.
- [37] T. Ikuno, H. Okamoto, Y. Sugiyama, H. Nakano, F. Yamada, I. Kamiya, Electron transport properties of Si nanosheets: transition from direct tunneling to Fowler-Nordheim tunneling, Appl. Phys. Lett. 99 (2011) 1–4, https://doi.org/10.1063/ 1.361.0486
- [38] S.H. Yoon, S.H. Kim, D.Y. Kim, Correlation between I (current)-V (voltage) characteristics and thermally stimulated depolarization current of Mn-doped BaTiO₃ multilayer ceramic capacitor, J. Appl. Phys. 114 (2013), 074102, https://doi.org/10.1063/1.4818947.
- [39] C.J. Peng, H. Hu, S.B. Krupanidhi, Electrical properties of strontium titanate thin films by multi-ion-beam reactive sputtering technique, Appl. Phys. Lett. 63 (1993) 1038–1040, https://doi.org/10.1063/1.109827.
- [40] N. Meng, X. Ren, X. Zhu, J. Wu, B. Yang, F. Gao, H. Zhang, Y. Liao, E. Bilotti, M. J. Reece, H. Yan, Multiscale understanding of electric polarization in poly (vinylidene fluoride)-based ferroelectric polymers, J. Mater. Chem. C 8 (2020) 16436–16442, https://doi.org/10.1039/d0tc04310a.
- [41] M. Oshikiri, Y. Imanaka, F. Áryasetiawan, G. Kido, Comparison of the electron effective mass of the n-type ZnO in the wurtzite structure measured by cyclotron resonance and calculated from first principle theory, Phys. B Condens. Matter 298 (2001) 472–476, https://doi.org/10.1016/S0921-4526(01)00365-9.
- [42] J. He, Metal Oxide Varistors, Wiley-VCH, Weinheim, Germany, 2019, https://doi. org/10.1146/annurev.ms.17.080187.001503.
- [43] G. Blatter, F. Greuter, Carrier transport through grain boundaries in semiconductors, Phys. Rev. B 33 (1986) 77–86, https://doi.org/10.1142/ 9789812816733 0006.